Routing information flow by separate neural synchrony frequencies allows for "functionally labeled lines" in higher primate cortex

Mohammad Bagher Khamechian[a], Vladislav Kozyrev[b,c,1], Stefan Treue[b,c,d,e,2,3], Moein Esghaei[b,f,3], and Mohammad Reza Daliri[a,f,2,3]

[a]Neuroscience and Neuroengineering Research Laboratory, Biomedical Engineering Department, School of Electrical Engineering, Iran University of Science and Technology (IUST), Narmak, 16846-13114 Tehran, Iran; [b]Cognitive Neuroscience Laboratory, German Primate Center – Leibniz Institute for Primate Research, 37077 Goettingen, Germany; [c]Bernstein Center for Computational Neuroscience, 37077 Goettingen, Germany; [d]Faculty of Biology and Psychology, University of Goettingen, 37073 Goettingen, Germany; [e]Leibniz-ScienceCampus Primate Cognition, 37077 Goettingen, Germany; and [f]School of Cognitive Sciences, Institute for Research in Fundamental Sciences, 19395 Tehran, Iran

Edited by Terrence J. Sejnowski, Salk Institute for Biological Studies, La Jolla, CA, and approved April 30, 2019 (received for review November 21, 2018)

Efficient transfer of sensory information to higher (motor or associative) areas in primate visual cortical areas is crucial for transforming sensory input into behavioral actions. Dynamically increasing the level of coordination between single neurons has been suggested as an important contributor to this efficiency. We propose that differences between the functional coordination in different visual pathways might be used to unambiguously identify the source of input to the higher areas, ensuring a proper routing of the information flow. Here we determined the level of coordination between neurons in area MT in macaque visual cortex in a visual attention task via the strength of synchronization between the neurons' spike timing relative to the phase of oscillatory activities in local field potentials. In contrast to reports on the ventral visual pathway, we observed the synchrony of spikes only in the range of high gamma (180 to 220 Hz), rather than gamma (40 to 70 Hz) (as reported previously) to predict the animal's reaction speed. This supports a mechanistic role of the phase of high-gamma oscillatory activity in dynamically modulating the efficiency of neuronal information transfer. In addition, for inputs to higher cortical areas converging from the dorsal and ventral pathway, the distinct frequency bands of these inputs can be leveraged to preserve the identity of the input source. In this way source-specific oscillatory activity in primate cortex can serve to establish and maintain "functionally labeled lines" for dynamically adjusting cortical information transfer and multiplexing converging sensory signals.

macaque area MT | computational modeling | neural oscillations | high gamma | local field potential

Complex neural tasks such as converting sensory information into appropriate motor actions and the associated decision processes require carefully and dynamically coordinated neural activity in networks of cortical areas (1–5). Many studies have shown that the response variability of the contributing populations of sensory neurons play a central role in determining the variations of behavioral response (6–18), as well as perceptual decisions (19–21). Local field potentials (LFPs)—signals representing the extracellular neural activity in a local volume of brain tissue—provide a measure for activities mediated by relatively localized neuronal pools (22, 23). These signals, extracted from the low-frequency (<500 Hz) components of extracellular neural signals, reflect mainly the collective synaptic activities across local neural populations (23, 24), predominantly induced by the local spiking activity (25). Recent research has shown that LFP signals could provide useful information on how neural activities are linked to behavior (12, 14, 16, 17, 26). These studies have demonstrated that the power of gamma and high-gamma (50 to 200 Hz) LFPs, as well as multiunit neural activities, in area MT of primate visual cortex are linked to behavioral outputs in a trial-by-trial manner (14, 16). Moreover, the strength of gamma synchrony induced among MT neurons reflects the size of correlation between neural activity and behavior (12). Interestingly, it has also been shown that the degree of gamma-band synchronization among activated V4 neurons can predict the speed of behavioral responses (17). Many studies thereby have linked multiunit activities, as well as the neural oscillations captured by LFPs, to behavior. However, it is not clear, especially for area MT (an area with strong projections to motor cortical areas), how single neurons are temporally coordinated relative to either an area's input neural activity or its overall population activity, to modulate behavior.

Temporal coordination of single neurons in a neuronal ensemble is often measured by the coupling of spiking activities to LFP oscillations (27–31). Such a coupling has been observed over many cortical regions, such as visual areas (28, 32–34), the prefrontal cortex (35), motor cortex (29), and hippocampus (30, 36–38).

Here, we have taken advantage of the coupling between single-unit activities and the LFP phases to study how the temporal coordination of single neurons in area MT of rhesus monkeys may be associated to the animal's behavior. Our results

Significance

Dynamical coordination of the neural activity between individual neurons is known to have a key role in the efficient transfer of sensory information to associative areas. Here, we report a role of interneuronal synchrony within the high-gamma (180 to 220 Hz) frequency range of activity in macaque area MT (a visual area in the dorsal visual pathway) in determining behavioral performance. This is, however, in contrast to previous reports for the ventral visual pathway (such as area V4), where only gamma range (40 to 70 Hz) was observed to play a role. We propose that such a difference between the functional coordination in different visual pathways might be used to unambiguously identify the source of input to the higher areas.

Author contributions: M.B.K., S.T., M.E., and M.R.D. designed the study; V.K. and M.R.D. recorded the data; M.B.K. performed data analyses; M.B.K., S.T., M.E., and M.R.D. interpreted the data; and M.B.K., S.T., M.E., and M.R.D. wrote the paper.

The authors declare no conflict of interest.

This article is a PNAS Direct Submission.

The data underlying the result figures are publicly available on figshare (https://doi.org/10.6084/m9.figshare.8160029).

[1]Present address: Laboratory of Systems Neuroscience and Imaging in Psychiatry (SNIP), University Medical Center Goettingen, 37099 Goettingen, Germany.

[2]To whom correspondence may be addressed. Email: treue@gwdg.de or daliri@iust.ac.ir.

[3]S.T., M.E., and M.R.D. contributed equally to this work.

This article contains supporting information online at www.pnas.org/lookup/suppl/doi:10.1073/pnas.1819827116/-/DCSupplemental.

Published online May 30, 2019.

indicate that, while an animal performs a visual change detection task, the coupling of spikes to high-gamma LFP oscillations (>180 Hz) in the dorsal visual pathway predicts the animal's behavioral responses. This suggests that efficient sensory information processing is aided by a high degree of coupling between the input from an upstream area to a cortical area's output. Given a similar observation, but in a different frequency band [gamma oscillations (40 to 70 Hz)] along the ventral visual pathway, we propose that downstream cortical areas may use these distinct frequency bands to distinguish input from the two pathways using these "functionally labeled lines."

Results

To study the neural mechanisms underlying visuomotor behavior, we trained three monkeys to perform a change detection task (*SI Appendix*, Fig. S1). Each monkey had to touch a lever and maintain its gaze on a central fixation point to start a trial. Next, an eccentric spatial cue briefly appeared on the screen to mark the upcoming target stimulus' location. Then, two (monkeys H and T) or four (monkey C) coherently moving random dot patterns (RDPs) were shown and the monkey was rewarded with a drop of juice if it released the lever immediately after the target RDP underwent a short color/direction change. All animals correctly reported the target change in more than 85% of those trials which were not terminated because the gaze deviated from the fixation point. Single-unit activity and LFPs were recorded simultaneously from area MT of the three monkeys while they performed the task. Each animal's hit trials were sorted into two subsets according to its reaction time to the target change [response time (RT)] distribution. To this end, the trials were sorted based on their RTs in an ascending order and subdivided into four partitions based on the thresholds corresponding to 25% quantiles. An equal number of trials were selected from the first and last partitions to create a "fast" and "slow" subgroup of trials. Here we measure the interneuronal synchronization by calculating the coupling of neural spikes to the phase of different LFP frequencies [spike-phase coupling (SPC)] (35, 39). SPC is computed for the neural activity in a 1,000-ms time window following the stimulus onset before the target change (see *SI Appendix*, Fig. S2 for details). Our analyses demonstrate that SPC in high-gamma frequencies (180 to 220 Hz) is locally enhanced during fast trials.

SPC in High Gamma Accelerates Behavior. The SPC allows us to quantify the coupling of neural spikes to the LFP phase. The magnitude of SPC lies between [0, 1]; it equals 1 when spikes occur only at a certain phase of LFP, while it is 0 when spikes distribute in time independently of the LFP phase. To compare the SPC between fast and slow trials, we first equalized the number of spikes across the two trial sets to eliminate any statistical dependence of the SPC on spike count. To this end, we focused on those trials with an enough number of spikes and randomly selected an equal number of spikes among them. Trials with a small number of spikes were removed to maximize the number of spikes for our analyses for each monkey (*Methods*). By this, we came up with 67, 22, and 23 neurons for animals H, T, and C, respectively. Second, we filtered the LFPs into nonoverlapping 5-Hz-wide frequency bands with their lower bounds between 1 and 245 Hz. Third, we selected a subset of trials with no significant difference between the LFP power of the fast and slow trials in each frequency band [median significance $\rho > 0.9$, two-sided rank-sum test across 50 frequency bands (1:5:250 Hz) for the three monkeys; see *SI Appendix*, Fig. S3 for number of selected trials per frequency band]. This made us confident that differences of signal-to-noise ratio do not bias our comparison of fast and slow trials. Fourth, we applied a Hilbert transform on the filtered LFPs in each frequency band to compute the instantaneous phases. Finally, the SPC was calculated for each trial by averaging unit-length vectors with the same phase as the LFP at the time of spikes and measuring the length of the resultant vector in each frequency band. Fig. 1 *A*–*C* shows the SPC in each frequency band separated by RT. *x* axes represent the upper bound of the frequency bands and the *y* axes indicate the SPC for fast and slow trials (blue and red, respectively). These results clearly show that the single-unit activity in fast trials is more strongly locked to the LFP phase compared with slow trials, especially in the high-frequency range (180 to 220 Hz) (Fig. 1, blue vs. red traces; see *SI Appendix*, Fig. S4 for the time-resolved SPC) ($\rho < 0.0006$ two-sided sign test, controlled for multiple comparisons using Bonferroni correction). Moreover, this SPC difference is not caused by either sudden changes in LFP/spike rate (*SI Appendix*, Figs. S5 and S6), a correlation between spiking and high-gamma power (see *SI Appendix* for details), differences in the distribution of interspike intervals (*SI Appendix*, Fig. S7), the specific trial selection performed to equalize spectral powers (see *SI Appendix* for details), or LFP pattern differences between the two behavioral conditions (*SI Appendix*, Fig. S8). Also, removing the temporal pattern of spike trains eliminated the SPC difference (*SI Appendix*, Fig. S8). Further investigation of interneuronal synchrony indicated that spiking activity of neighboring neurons was synchronized significantly more in the high-gamma frequency range (180 to 220 Hz) for the fast rather than the slow trials ($\rho < 0.0075$, permutation test; see *SI Appendix*, *Supplementary Information Text* and Fig. S9 for details). Fig. 1*D* illustrates the distribution of the high-gamma LFP phase at the time of spikes (preferred phase) for fast and slow trials pooled across the three monkeys. Here we calculated the preferred phase for each trial by computing the circular average across the high-gamma phases simultaneous to the spikes (*Methods*). These histograms indicate that spikes selectively occur within a certain phase range in fast trials, while they are distributed randomly in slow trials ($\rho < 10^{-8}$, fast trials; $\rho > 0.07$, slow trials; Rayleigh test). We further found a significant difference between the two distributions' circular median [$\rho < 10^{-4}$, circular Kruskal–Wallis test (40)]. Along the same lines, to visualize the exaggerated phase locking in fast trials, we calculated the spike triggered average of the high-gamma LFP (STA_{HG}) in the fast and slow trials for monkey H (Fig. 1*E*, blue vs. red curves, respectively; see also *SI Appendix*, Fig. S10 for monkeys T and C). To compute STA_{HG} in a given trial, the LFPs were first high-gamma-band-filtered and next a ±30-ms segment of the LFPs surrounding each spike were extracted and averaged across spikes for each trial. The STA_{HG}s were next averaged across trials (*Methods*). The average STA_{HG} for fast trials shows a larger difference between the maximum and minimum magnitude ("peak-to-peak difference") compared with the slow trials. This suggests that spikes occur more selectively around the peak phase of the high-gamma LFP in fast (as shown by the black vector in the blue histogram, Fig. 1*D*) compared with slow trials. This locking of spikes to high-gamma LFP is similarly observed in the wide-band LFP (before applying any narrow band filtering; *SI Appendix*, Fig. S11).

SPC Influences Behavior Locally. We next investigated whether the behavioral RT depends selectively on the SPC of the neurons representing the target change or alternatively it depends equally on the SPC of neurons across the visual cortex. Therefore, we separately analyzed the trials where the target stimulus was shown inside or outside the receptive field (RF). For this analysis we focused on the data from animals H and T for which the target was shown in both locations [for animal C there was not a sufficient number of trials for the target-out condition (see the original task description in ref. 41)]. Following an equalization of the trials for the target position and RT conditions, we calculated the SPC in each condition. To measure how much SPC discriminates RTs, we calculated the area under the receiver operating

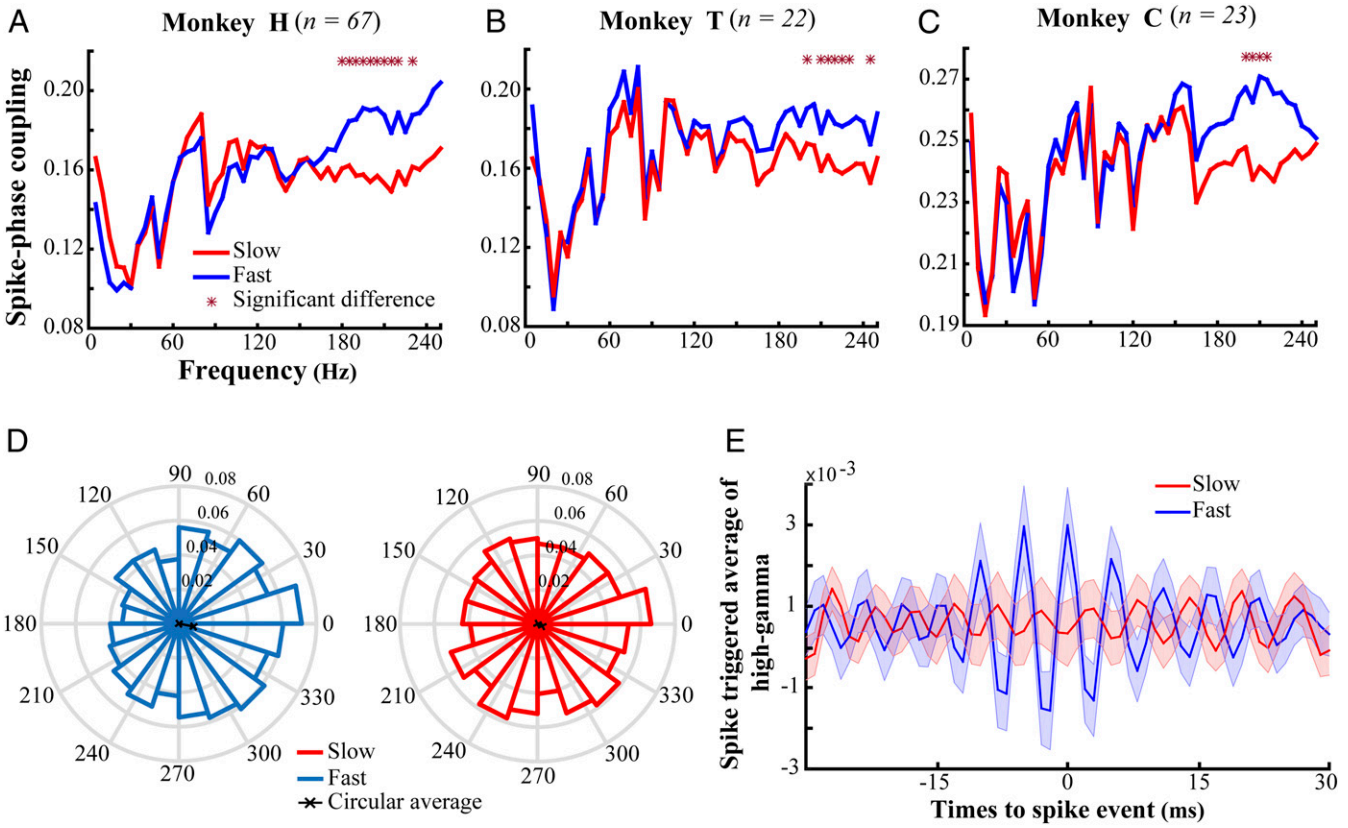

Fig. 1. SPC for trials with fast and slow RTs. (*A*–*C*) SPC of the fast and slow trials across different frequency bands with a width of 5 Hz spaced by 5 Hz, for monkeys H, T, and C. *x* axes indicate the upper bound of these frequency bands, and *y* axes represent the SPC values. Stars mark the frequencies with a significant difference between fast and slow trials ($\rho < 0.0006$ two-sided sign test, corrected for multiple comparisons using the Bonferroni method). (*D*) The histogram of spike-triggered high-gamma (180 to 220 Hz) phases across trials for the two trial types pooled across all of the three monkeys ($\rho < 10^{-8}$, fast trials; $\rho > 0.07$, slow trials; Rayleigh test). The black lines show the average phase across trials. (*E*) The spike-triggered average of high-gamma frequencies (180 to 220 Hz) for the two types of trials for monkey H's data. Error bars represent the SEM. Red and blue represent the slow and fast trials, respectively. *n* indicates number of neurons analyzed for individual animals.

characteristic (ROC) curve (AUC) between the SPCs of fast and slow trials, for each target position condition (*Methods*). Fig. 2 shows the AUCs for those high-gamma frequencies which discriminate the reaction times (as shown in Fig. 1 *A*–*C*) for monkeys H and T. Comparison of the two target-position conditions shows that AUCs of the target-in condition are significantly larger than that of the target-out condition ($\rho < 0.05$, permutation test) (see SPCs in the target-out condition in *SI Appendix*, Fig. S12). This suggests that a neuron's coupling to the high-gamma LFP phase contributes to visuomotor processing preferably for those stimuli which selectively drive the neuron, rather than any stimulus regardless of its properties.

Spike–High-Gamma Coupling Is Dissociated from Spectral Leakage of Spike into LFP. An important concern in terms of the link between spikes and high-gamma LFP is that lower-frequency components of a spike's waveform may leak into neighboring LFP (14, 42). This leakage could cause an artificial coupling between spikes and the LFP phase. To investigate if our calculation of SPC simply reflects this leakage or an actual coupling between spikes and the synaptic activity captured by LFP we took the three approaches discussed below.

SPC strength does not decrease relative to the distance between spike-providing and LFP-providing electrodes. To test if the SPC we observed is due to the spectral leakage of spikes onto LFP we investigated if the coupling of spikes to high-gamma LFP depends on the distance between the spike-providing and LFP-providing electrode. In case of a spurious SPC, the magnitude of coupling has been shown to decrease with an increased distance between spike-providing and LFP-providing sites (43). We calculated the average STA_{HG} across all trial types by taking the spikes and LFPs from the same or separate electrodes. Fig. 3*A* plots the peak-to-peak amplitude difference of the average STA_{HG} (as a measure of spike–LFP coupling) with the spikes and LFP from a single electrode (interelectrode distance = 0) or pairs of electrodes with different distances in between (STA_{HG} for each interelectrode distance is shown in *SI Appendix*, Fig. S13*B*). As shown in the figure, these peak-to-peak amplitude differences do not decrease (and even slightly increase, $0.01 < P < 0.05$, Pearson correlation) by the increase of interelectrode distance, confirming that the observed SPC is not an artifact of a spectral leakage from spikes onto LFPs (*SI Appendix*, Fig. S13*C*). Nevertheless, one potential reason for the large amplitude difference of STA_{HG} for interelectrode distances of 3–4 (compared with that of distances 0–2) could be the low data size (average trial numbers: 11 for distances 3–4 vs. 169 for distances 0–2), leading to a large variability across repetitions of STA_{HG} calculation and an unreliable measurement of the average STA_{HG}.

Behavioral dependence of SPC is dissociated from the spike–LFP leakage. To evaluate if it is the spectral leakage of spikes onto LFP that induces the dependence of SPC on RT, we selected two subsets from the fast trials which are significantly different in their high-gamma SPC (Fig. 3*B*) ($\rho = 0.00031$, two-sided rank-sum test across the peak-to-peak amplitude difference of the STA_{HG}s) (*Methods*). We next calculated the spike-triggered average LFP (STA_{LFP}) for each of the trial subsets by averaging the LFP segments in a ±10-ms time interval surrounding each spike [the interval with the maximally observed SPC strength in high

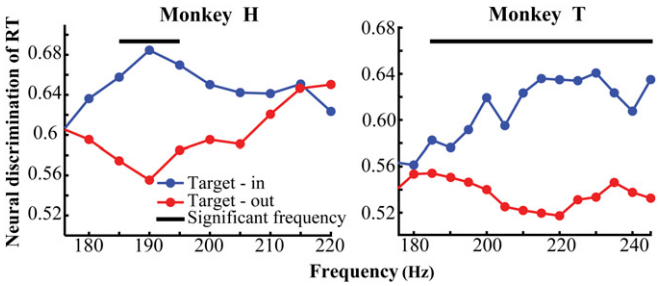

Fig. 2. Neural discrimination of RT based on high-gamma SPC for targets inside and outside the RF. The *y* axes represent the area under the ROC curve when comparing fast and slow trials over the two target position conditions for monkeys H and T. *x* axes show the lower bound of the frequency bands under study. The black lines show the frequency bands with a significant difference in the neural discrimination of RT between target-in and target-out trials ($\rho < 0.05$ permutation test, corrected for multiple comparisons).

gamma (*SI Appendix*, Fig. S11; also see refs. 14 and 42)] (Fig. 3*C*). We quantified the overall leakage of spikes onto LFP by computing the peak-to-peak amplitude difference of the STA_{LFP}s and found no statistically significant difference between that of the two trial subsets ($\rho = 0.0588$, two-sided rank-sum test). This suggests that the magnitude of SPC in high-gamma frequencies is independent of the spike's leakage onto LFP.

Behavioral dependence of SPC. Finally, our documented dependence of SPC on RT cannot be attributed to differences in the magnitude of spike leakage, since we eliminated here for any differences in spectral band power and spike number between the fast and slow trials (*Methods*). This rules out any systematic difference in SPC of the two trial types. Therefore, the high-gamma SPC difference between the fast and slow trials reflects a difference of SPC between them, rather than a difference of spike leakage.

Functionally Labeled Lines Distinguish Input Source. Our data suggest that the strength of coupling between spikes and the LFP phase within the range of high-gamma (180 to 220 Hz) frequencies predicts the behavioral speed. We speculate that this coupling, which is a more reliable predictor of the animal's reaction time compared with spike rate (*SI Appendix*, Fig. S14), might have a role in efficient information transmission to downstream areas. A similar finding in area V4 (which is the only study that has examined the role of oscillations in a detection task within the ventral visual pathway) describes such a coupling within a different frequency band of LFPs [gamma (40 to 70 Hz)] (17). Since this frequency difference could not be attributed to differences between the tasks/areas of the two studies (see *SI Appendix* for details), here we hypothesize that the two pathways in primate visual cortex use different frequency ranges to propagate information, enabling downstream association areas to distinguish the source of incoming spikes (Fig. 4 *A* and *B*).

There is no straightforward way for a neuron in a downstream associative cortical area [such as the prefrontal cortex (PFC)] receiving inputs from the ventral and dorsal pathways (e.g., V4 and MT) to distinguish the source of incoming spikes. We hypothesize that down-stream neurons (like PFC neurons) are at least of two different types; in some the dendritic membrane potential fluctuates within the range of gamma (40 to 70 Hz) frequencies and in the other, within the range of high-gamma (180 to 220 Hz) frequencies. Given that a neuron generates an action potential only when its rest membrane potential (which is by itself oscillating) passes the firing threshold, the neuron is more likely to fire when the incoming spike coincides with the membrane potential's peak phase of the characteristic frequency. Assuming that the dendritic oscillatory activity in each of the two neuron types is synchronized to that of the corresponding upstream area (MT and V4 in this case), each neuron will generate an action potential only in response to those incoming spikes that are locked to the preferred phase of the receiving neuron's characteristic frequency. Correspondingly, each of the two neuron types specifically extracts the spikes originating from either MT or V4 (Fig. 4*C*). We used a minimalistic model to show this to be physiologically plausible.

First, we assumed two PFC neurons where their membrane potential oscillates (either via resonance or interneuronal coupling) following a sinusoid ([0 1]) with a frequency of either 55 Hz (gamma) or 200 Hz (high gamma). This means that these neurons are more likely to generate a spike when receiving an input spike during the high excitability phases (i.e., peaks of the corresponding oscillation). This phenomenon is known as "stochastic resonance" in the modeling literature, where the spontaneous oscillation (here, gamma/high gamma) is taken as the intrinsic resonating component of the membrane potential, and input spikes are considered as the stochastic noise entering the cell (ref. 44, chap. 6, and refs. 45 and 46). We further set these model neurons to generate a spike when they reach a threshold (0.8). Second, we generated 800 random spike trains (1,000-ms length, 80 spikes) each containing spikes either from MT, V4, both or none (40 spikes to represent information from each of V4 and MT, interleaved and 200 spike trains for each of the above four conditions). Each of MT's and V4's spikes were randomly assigned times, so they would be phase-locked to the high gamma's or gamma's peak (as their preferred phase), respectively. For this, we made sure that at least 80% of the generated spikes co-occur with the oscillations' peaks (see *SI Appendix*, *Supplementary Information Text* and Fig. S15 for a demonstration of these data). Third, we fed the generated spike trains into the two modeled PFC neurons and measured the number of their output spikes in each of the four conditions (Fig. 4*D*). As clearly shown in the figure, for a given

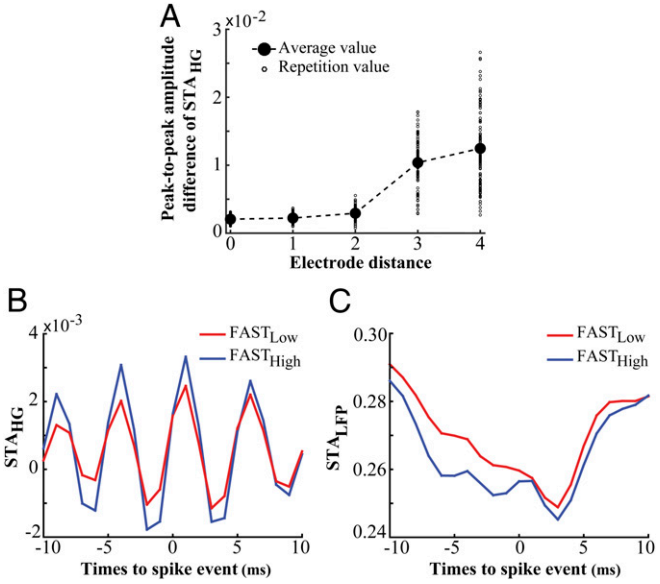

Fig. 3. Spike–LFP coupling in high gamma is not due to the "leakage" of spike waves into the LFP. (*A*) The peak-to-peak amplitude difference of averaged STA_{HG} for electrode pairs with different distances. The averaged STA_{HG} was computed using the spike and LFP coming from the same (distance = 0) or separate electrodes (distances 1–4). The small and large circles indicate the peak-to-peak amplitude difference of the averaged STA_{HG} for each repetition and the average across repetitions, respectively. (*B*) The average STA_{HG} for the two extreme subsets of fast trials ($FAST_{Low}$ vs. $FAST_{High}$) ($\rho = 0.00031$, two-sided rank-sum test). (*C*) The average STA_{LFP} (spike-triggered LFP based on raw LFPs) for $FAST_{Low}$ and $FAST_{High}$ trials, showing no significant difference between their peak-to-peak amplitude differences ($\rho = 0.06$, two-sided rank-sum test). These analyses were done for monkey H.

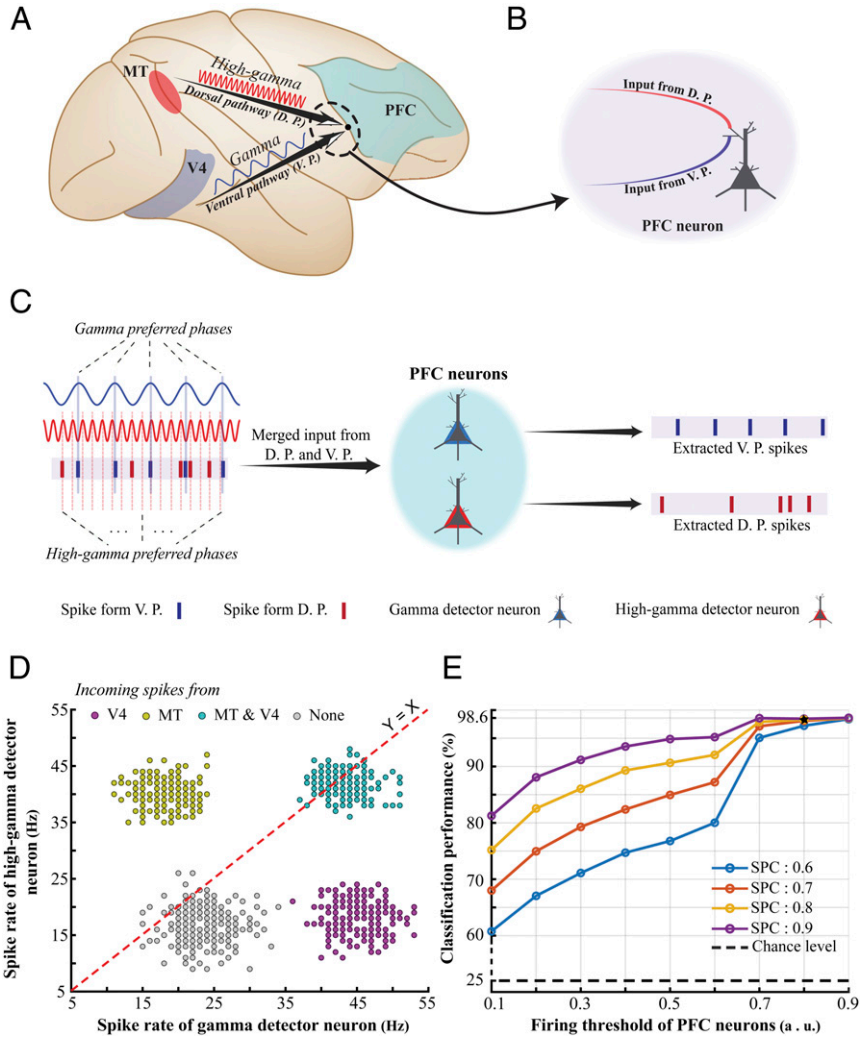

Fig. 4. Using "functionally labeled lines" to distinguish information coming via the dorsal vs. ventral visual pathway. (*A*) Schematic description of our "functionally labeled lines" hypothesis. We propose that the dorsal and ventral visual pathways use different characteristic frequencies, enabling higher-order association areas (such as the PFC) to distinguish the information coming from each pathway. (*B*) A PFC neuron that is targeted by axons originating from the ventral and dorsal pathways (V4 and MT, respectively, for instance) is not capable of distinguishing the source of individual incoming spikes, if it is confined to a simple summing compartment of inputs. (*C*) Suggested by empirical data, each visual pathway propagates information using spikes that are phase-locked to a different frequency range. We suggest that this mechanism enables the downstream neurons to filter out the incoming spikes based on the frequency they are phase-locked to. We hypothesize that PFC neurons have either of the following distinct properties: Some oscillate in their dendritic potentials within the range of gamma (40 to 70 Hz) (named "gamma detector neurons" here) and the others in the range of high gamma (180 to 220 Hz) (named "high-gamma detector neurons"). Assuming that the dendritic oscillatory activity in each of the two neuron types is synchronized to that of the corresponding upstream area (MT and V4 in this case), each neuron will pass its threshold voltage, generating an action potential only in response to those incoming spikes that are locked to the preferred phase of the neuron's characteristic frequency. Correspondingly, each of the two neuron types specifically extracts the spikes originating from either MT or V4. (*D* and *E*) We modeled the four conditions where incoming spikes are phase-locked to gamma only (representing input only from V4), high gamma only (representing input only from MT), both (representing input from both areas), and none (representing input from none of the areas). As shown in *D*, the response of the PFC's gamma detector and high-gamma detector neurons (*x* and *y* axes, respectively) together clearly distinguish each of the four conditions, indicating the source of the incoming spikes (MT or V4). Assessing the accuracy of distinguishing these four conditions by an ideal observer (*E*) shows that PFC neurons could identify the source(s) within a wide range of physiological parameters [firing threshold (*x* axis) and SPC strength (colors)].

spike train received from MT and V4 together, the combination of outputs from the PFC model neurons could discriminate the origin of the incoming spikes (whether incoming spikes originate from MT, V4, both, or none).

To measure the robustness of the model's performance in distinguishing the above four conditions across different firing thresholds and SPC strengths we used a support vector machine (SVM) classifier [LIBSVM toolbox (47)] to discriminate the four classes of incoming spikes from incoming spikes from V4, MT, V4 and MT, and none, based on the spike trains generated by the PFC's gamma and high-gamma detector neurons. We generated 200 trials for each of the four classes and calculated the spike rate generated by the two types of PFC neurons. We used 70% of the total trials (560 trials) for training the SVM and the remaining trials for test. Fig. 4*E* shows the classification performance (*y* axis) across different firing thresholds (*x* axis) and different SPC strengths. Our model shows a considerable accuracy even under noisy conditions where the firing threshold and SPC had the lowest values. Our model therefore indicates that the functionally labeled lines using characteristic oscillation frequencies may help associative areas distinguish neural inputs from different upstream areas.

In conclusion, we showed here that SPC in high-gamma frequency band is a predictor of the behavioral response speed in detecting the visual target change (i.e., a higher high-gamma SPC

induces a faster response by the monkey). Our results suggest a local neural mechanism for controlling an efficient visuomotor processing in the dorsal visual pathway. Given that the ventral visual pathway uses a different frequency band than the dorsal pathway, we propose that higher cortical areas might take advantage of this difference to functionally label lines coming via the dorsal vs. the ventral visual pathway.

Discussion

The synchronization of neural assemblies has been reported across brain areas for different species (28, 48–55). However, the functional role of this synchrony in the context of cognitive processes has remained elusive. Here, we studied the role of interneuronal synchrony in the generation of behavioral responses by rhesus monkeys. Our results show, first, that the magnitude of neural synchrony in high-gamma (180 to 220 Hz) frequencies predicts the monkey's speed in reporting the change of a target stimulus and that the coupling of spikes to the high-gamma LFP's phase predicts the behavioral RTs. This suggests that the likelihood of spikes to occur at a specific phase of LFP (the preferred phase) is more pronounced in trials with fast compared with slow responses (see Fig. 5 for a schematic illustration). Second, the magnitude of this synchrony indicates how efficient neurons process the stimulus presented inside their receptive field. These suggest that in rhesus monkey visual cortex neuronal synchrony for frequencies as high as the high-gamma band may be functionally important in visuomotor behavior. Third, associative cortical areas could distinguish the source of incoming inputs, using the characteristic transmission frequency range of each input, supporting previous reports of a similar mechanism for the communication between other brain regions (37, 56). For instance, a study of the entorhinal–hippocampal system has indicated that different frequency bands within the broadband gamma (25 to 140 Hz) in CA1 were differentially phase coupled to the entorhinal cortex and CA3, suggesting that CA3 uses the slow (~25 to 50 Hz) and entorhinal cortex uses the fast (~65 to 140 Hz) frequency components to communicate with CA1 (56).

One measure of synchrony between neurons is spike–LFP coupling (39, 57), which has been shown to capture the synchrony of a single neuron to the synaptic activity in the surrounding population (58) in multiple brain areas (29, 30, 32, 33, 35, 37, 59).

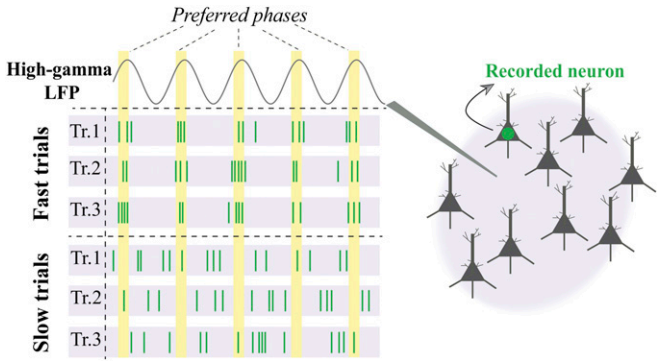

Fig. 5. The role of high-gamma synchrony in visuomotor behavior. Visualization of differential high-gamma phase synchrony for fast vs. slow behavioral responses. Spikes in three sample imaginary trials with fast (*Top*) behavioral responses show how the single neuron activity is coordinated in time (*x* axis), being locked relative to a specific preferred phase of the simultaneously recorded high-gamma LFP (*Right*). Conversely, the spikes recorded in trials with long RTs (*Bottom*) are distributed in time irrespective of the preferred LFP phase. We hypothesize that higher SPC leads to faster behavioral responses, via either coordination of MT input to its output neural activity or enhancing the efficacy of the neural projections from MT to downstream areas (*Discussion*).

This coordination has been proposed as the core solution to the problems of consciousness and binding—how visual features encoded in different brain regions are integrated to form a unified percept (54, 60, 61). Several studies have indicated that the neural activity–behavior correlation can be mediated by changes of firing rate (6, 8, 16, 19) or the spectral high-gamma power (14, 16, 42). Along these lines, some have documented a correlation between spiking activity and broadband high-gamma power for frequency ranges of 40 to 100 Hz (62) or 40 to 130 Hz (63), in a range of cortical areas, especially in humans (64). Our results demonstrate that the coupling of spikes to the phase of high-gamma oscillations (SPC) is a predictor of behavioral speed, independently of the population firing rate or spectral high-gamma power. Moreover, previous studies have documented that gamma oscillations are linked to stimulus properties (size, speed, or contrast) (14, 65–67). Since our experiments did not involve systematic changes of stimulus sensory properties, either across trial types or within our analysis window in a given trial, the observation of high-gamma SPC's variation with RT cannot be attributed to such sensory properties. Furthermore, our observation of a SPC–behavior link for different animals with different task properties, and independent of stimulus properties (size and number) (*Methods*), suggests that high-gamma SPC is a generalizable oscillatory neural component underlying visuomotor change detection.

We found for one of our monkeys that spikes slightly preceded the peak phase (rather than the trough) of the high-gamma cycle. The peak phase has been reported to correspond to the highest magnitude of information (as well as the lowest noise correlation) within the gamma cycle (34). Given the similarity of the preferred phase between low and high gamma frequency ranges (50 to 200 Hz; supplementary figure 5 of ref. 43), we expect that the peak phase in high gamma similarly corresponds to the highest sensory information. Nevertheless, future studies need to examine this.

The Role of Neural Response Variations in Creating Neural Synchrony. Previous studies on the neural mechanisms underlying behavior have revealed at least two components to the trial-to-trial neural variability in the activity within a sensory area. The first is a "shared component" attributed to the top-down or bottom-up synaptic input to the sensory population; the second is an "independent component" that is not induced by either the upstream or downstream areas, presumably arising from the stochastic nature of spiking of individual sensory neurons, or the interaction within the local cortical circuit of the sensory area (13, 68, 69). This independent component is suggested as a core determinant of the behavioral latency (13). Based on our observations, we suggest the following hypothesis as to how the local neural activity shapes behavior: Given that phase locking of single neurons to the LFP reflects the degree of interneuronal synchrony, the more synchronous the MT neurons are, the higher the likelihood of influencing the downstream neuron's output, and consequently the more efficient the propagation of relevant information toward downstream visuomotor areas (both associative and higher-order visual areas) (28). This locking of the timing of single neurons to the LFP phase (reflecting the surrounding population's state) would enhance the gain of the downstream neuron, suggesting that the behaviorally relevant information is processed locally and then transferred to downstream areas. In other words, the synchrony of neurons engaged in stimulus processing decreases the stochastic activity or additive noise, and therefore the weight of the "independent neural component." This enhances the "shared component" reflecting the stimulus information representation with downstream associative/integrative areas (an increase of the shared/independent ratio). Together, these two neural processes enhance the transfer of information and its integration in associative/decision-making areas, improving behavioral outcomes.

Similar to our approach, a previous study (17) showed that the synchrony of V4 neurons in the gamma band (40 to 70 Hz) predicts the RT in reacting to an upcoming visual change, with a more powerful gamma band synchrony, correlated with a faster RT. They suggested therefore that the ventral visual pathway relays the relevant information via gamma synchrony (corresponding to a time window of ∼17 ms). However, our data show for MT that RTs are significantly linked to the high-gamma synchrony (180 to 220 Hz) [corresponding to a shorter time window (∼5 ms)] but not significantly linked to gamma band synchrony. This suggests that dorsal and ventral visual pathways use different time windows for interacting with their (similar) downstream areas, possibly to avoid any collision of information propagated into the destination area by the two streams, enabling the downstream area to maintain information on the source of each stream (Fig. 4). It could be argued that the observation of different frequencies in the two pathways is due to differences between studies done in different laboratories. Although we believe the results to be robust across differences in firing rates and monitor refresh frequencies (see *SI Appendix* for details), other sources of variation (such as interindividual differences, different recording hardware, and different analysis techniques) could conceivably affect the determination of the main frequencies. Duplication of the findings of Womelsdorf et al. (17) or of our findings in other laboratories as well as studies with simultaneous recording from the dorsal and ventral visual cortex in the same animal would be ways to determine the robustness of the distinct frequencies in the two visual pathways.

It is also possible, given that LFPs are a correlate of the synaptic input to an area (here area MT), a stronger coupling between the shared component of variation (reflected by the high-gamma dynamics) and a neuron's output accelerates the behavioral response. This implies that the stronger the input to MT impacts its output, the faster the behavior would be. However, the mechanisms strengthening this impact of inputs on single neurons' output remains a question for future studies.

The Origin of Cortical High-Gamma Oscillations and Their Functional Role in Cortical Processing. Previous investigations, mostly in rodents and humans, have extensively studied the neural basis of high-gamma oscillations and their links to cognitive functions. These findings suggested that intrinsic properties of interneurons generate high-gamma oscillations during transient ripples in rat (70–72) as well as human hippocampus (73, 74). It has frequently been suggested that interneurons contribute to the generation of these high-gamma oscillations in LFPs (48, 65, 75–78). Also, it has been observed that the high-gamma oscillation observed during sensory cortical activation reflects the population activity of inhibitory fast-spiking interneurons. This activity then imposes a rhythmic inhibition on excitatory pyramidal cells to also discharge in phase with the population rhythm, but at a lower rate (78). Furthermore, previous studies have shown that the ripple activities (or high-gamma oscillations), produced by local cortical circuits (76, 79), play a functional role in high-level cognitive functions, such as planning (80), decision making (81), and memory consolidation (82). For instance, Kucewicz et al. (83) showed that network oscillations in gamma frequencies (50 to 125 Hz) and above (>125 Hz) occur within the primary visual cortex, limbic, and higher-order cortical regions at the time of memory encoding and recalling.

Despite the role of high-gamma range neural activities in rodents and humans, it has frequently been suggested that they do not play a prominent role in monkey sensory cortex (especially visual cortex) (12, 84, 85) (but see ref. 78), instead proposing that these frequency components are due to a "spike bleed-through." Our results, however, show that this is not the case for macaque visual cortex [compare the blue curve in Fig. 1*E* with the high-gamma ripples observed in hippocampus (see figure 2 of ref. 70)], suggesting a mechanism for these oscillations similar to that in other mammals (as pointed out above). Nevertheless, these high-frequency fluctuations are widely observed to be locked to low-frequency (<20 Hz) oscillations (2, 86), leaving for future studies the question of to what extent synchrony in high frequencies independently controls behavior (87).

Furthermore, the physiological high-gamma oscillations show different properties compared with that of the pathological high-gamma oscillations observed in epilepsy patients. Pathological oscillations have a higher mean spectral amplitude, longer mean duration, and lower mean frequency than physiologically induced oscillations (88). Nevertheless, intracranial recordings even from epilepsy patients have shown the physiologically induced high-frequency oscillations during behavioral task experiments (89).

In summary, our empirical and modeling data suggest, first, that the magnitude of neural synchrony in high gamma frequencies (180 to 220 Hz) predicts the speed in reporting an upcoming change of a target stimulus. Second, this synchrony reflects the responsiveness of a neuron only to the stimulus presented inside the receptive field, suggesting an important role of high-gamma neural synchrony in the dorsal visual pathway's neural circuitry for the efficient processing of sensory information. Third, higher cortical areas could make use of the different characteristic frequencies used within the dorsal and the ventral pathways to build and maintain "functionally labeled lines" for controlling information transmission and multiplexing converging sensory signals (Fig. 4).

Methods

Animal Welfare. The scientists in this study are aware of and are committed to the great responsibility they have in ensuring the best possible science with the least possible harm to any animals used in scientific research (90). All animal procedures in this study were approved by the responsible regional government office (Niedersaechsisches Landesamt fuer Verbraucherschutz und Lebensmittelsicherheit) under permit numbers 33.42502/08-07.02 and 33.14.42502-04-064/07. The animals were group-housed with other macaque monkeys in facilities of the German Primate Center in Goettingen, Germany in accordance with all applicable German and European regulations. The facility provides the animals with an enriched environment, including a multitude of toys and wooden structures (91, 92), natural as well as artificial light, and exceeds the size requirements of the European regulations, including access to outdoor space. Surgeries were performed aseptically under gas anesthesia using standard techniques, including appropriate perisurgical analgesia and monitoring to minimize potential suffering (93). The German Primate Center has several staff veterinarians that regularly monitor and examine the animals and consult on procedures. During the study the animals had unrestricted access to food and fluid, except on the days where data were collected or the animals were trained on the behavioral paradigm. On these days the animals were allowed unlimited access to fluid through their performance in the behavioral paradigm. Here the animals received fluid rewards for every correctly performed trial. Throughout the study the animals' psychological and veterinary welfare was monitored by the veterinarians, the animal facility staff, and the laboratory's scientists, all specialized in working with nonhuman primates. The three animals participating in this study were healthy at the conclusion of our study and were subsequently used in other studies.

Experimental Task and Recordings. Three adult male monkeys (macaque) were trained to attend toward one of two (monkey H and T) or four (monkey C) coherently moving RDPs while ignoring the others (*SI Appendix*, Fig. S1). They initiated each trial by pressing a lever and simultaneously maintaining their gaze on a fixation spot centered on the screen. Subsequently, a cue was presented to signal the location of the upcoming target stimulus. The cue was either a static RDP presented in the same position of target stimulus for 455 ms (monkey H) or 500 ms (monkey T) or a moving RDP with the same location and direction for 600 ms (monkey C). Immediately after (for monkey T) or followed by a short blank period (for monkeys H and C), the moving RDPs were shown inside/outside the RF of the neuron under study, and the monkeys had to release the lever immediately after the target underwent a transient change. The change event for monkeys H, T, and C was a brief change in the direction, direction/color, or direction/speed, respectively, which occurred at a random time between 680 to 4,250 (monkey H), 400 to 2,500 (monkey C), or 500 to 3,550 ms (monkey T) following the stimulus onset.

For monkey H, the target and distractor's direction were the same, chosen randomly from eight possible directions (0 to 360° with steps of 45°). For monkey T, the RDPs moved toward either the preferred or null direction of the recorded neuron, and for monkey C the direction of motion for the RDP inside the RF was picked randomly from 12 possible directions (0 to 360° with steps of 30°). The monkeys were rewarded with a drop of juice for releasing the lever within the RT windows 150 to 650 ms (monkey H), 100 to 650 ms (monkey T), and 150 to 650 ms (monkey C) following the target change. In trials where the animals reported the distractor change, the trial was terminated without a reward. The animals correctly reported the target change at similar high rates, despite the differences in some task parameters, indicating similar levels of task difficulty. The hit rates were 86% (animal H), 90.3% (animal T), and 89% (animal C) of those trials which were not terminated because of an eye movement. All three animals performed a change detection task, maintaining fixation of a central point while covertly attending to a peripheral stimulus until it underwent a transient and abrupt change. Our selection of different task parameters (timing and stimulus properties) between the three animals ensured that a similar neural signature across monkeys cannot be attributed to a particular value for these parameters.

Single-unit activity (online sorted using Plexon's online sorter application) and LFP were recorded extracellularly from the area MT using a five-channel multielectrode recording system (Mini-Matrix, Thomas Recording, and Plexon data acquisition system, Plexon Inc.). For two of the monkeys (H and T), five parallel electrodes (with an interelectrode distance of 300 μm) and for the third monkey (C) one electrode was advanced into the brain tissue to isolate direction selective MT neurons with overlapping RFs. We recorded from 112 (monkey H), 30 (monkey T), and 27 (monkey C) sites in area MT. For more details on each of the animals' behavioral task, performance, and recording details see ref. 94 for monkey H, ref. 95 for monkey T, and ref. 41 for monkey C.

Neural-Behavioral Analysis. In the following, the details of our analyses are explained. All analyses were accomplished using MATLAB (MathWorks).

Trial-Selection Procedure. We focused on those trials where the monkeys correctly reported the target change. Regardless of the attention condition, the trials were sorted based on their RTs in an ascending order and subdivided into four partitions based on the thresholds corresponding to 25% quantiles. An equal number of trials were selected from the first and last partitions as fast and slow trials, respectively. The single-unit activity and LFP recordings in the fast and slow trials were selected for the next analysis. Our analyses were carried out over 590 to 1,590 ms (monkey H), 650 to 1,650 ms (monkey T), and 400 to 1,400 ms (monkey C) after stimulus onset, to ensure we are far enough from the stimulus-evoked responses due to the onset of motion stimuli (see *SI Appendix*, Fig. S2 for details). For all analyses, the power line 50-Hz noise was eliminated from LFPs using a Butterworth notch filter.

Analysis of SPC. SPC measures the phase synchronization between LFP and single-unit activities recorded from a single electrode. To eliminate any potential bias to spike rate, we randomly downsampled the spikes to equalize the spike numbers across trials [using a thinning (decimating) procedure (57, 96–98)]. Those trials with a small number of spikes were removed, to maximize the number of spikes for our analyses for each monkey. To this end, we calculated a threshold based on the average spike number within the analysis period for neurons from each monkey and discarded those trials with a spike count smaller than this threshold (39 for monkey H, 31 for monkey T, and 15 for monkey C). The SPC results did not qualitatively differ for other threshold values close to (±10) the thresholds we used. After thresholding, our dataset contained 67, 22, and 23 neurons for animals H, T, and C, respectively. Next, for those trials with more spikes than the threshold, we randomly removed enough spikes to reach the threshold.

The LFPs were fed into an FIR filter bank consisting of 5-Hz-wide band-pass filters ranging between 1 Hz to 250 Hz (without overlap). The EEGLAB toolbox (eegfilt function) was used for LFP filtering. It provided a narrowing roll off for stop-band using a filter order of 3 × (sampling_rate/low_cutoff_frequency). To avoid dependence on spectral power in the SPC analysis (98), a subset of the fast/slow trials with the same average spectral power was selected subsequently after filtering the LFPs. The trial selection was established using the histogram of band powers for fast/slow trials. To this end, first, we calculated LFP band power for each trial per frequency band (5-Hz bandwidth). Second, we calculated the histogram of LFP band powers and picked up the same number of trials per histogram bin from the fast and slow trials. The resolution of these histograms (bin size) was kept equal for fast and slow trials, and it was selected so as to provide two subsets of trials with no significant differences between fast and slow groups on each frequency band [median significance $\rho > 0.9$, two-sided rank-sum test across 50 frequency bands (1:5:250 Hz) for the three monkeys]. To this end, the difference between the minimum (zero) and maximum of a trial's band power was split into narrow bins for histogram calculation. The histogram bin size was 10^{-4}, 5×10^{-4}, or 10^{-4} arbitrary units (animals H, C, and T, respectively, for frequency bands lower than 150 Hz) or 2×10^{-5} arbitrary units (for higher frequencies). There were on average three (for animals H and C) or two trials (animal T) per histogram bin for shared bins of fast and slow trials. With this, the number of selected trials was also equal in both classes for each frequency band. Using this trial selection approach, initially there were (725,725), (461,461) and (208, 208) (fast, slow) trials for animals H, T, and C, respectively, out of which (251, 214), (192, 116), and (99, 138) trials were selected after applying the spike thresholding procedure. *SI Appendix*, Fig. S3 shows the number of selected trials in each frequency band for each monkey, after applying the spike thresholding and power equalization procedure. The selected trials were fed into a Hilbert transform to compute the instantaneous phase of the oscillations. Eventually, the SPC was calculated for the resulting trials with the same spectral band power and spike rate in both of the fast/slow trials. The SPC was computed for each trial by calculating the magnitude of the circular average of instantaneous phases simultaneous to the spikes:

$$\mathrm{SPC}\ (f) = \frac{1}{n}\left|\sum_{j=1}^{n} e^{i\omega t_j}\right|, \omega = \{\ 2\pi f | 0 \le f \le 250\ \mathrm{Hz}\}, -\pi \le \omega \le \pi, \qquad [1]$$

where n, f, t_j, and ω are the number of spikes, target frequency where LFP is filtered to, spike times, and instantaneous phases, respectively, in a given trial. The SPC magnitude lies between [0, 1], where 0 represents no coupling between the spikes and LFP phase and 1 indicates the maximum coupling.

Given the small number of trials/spikes for monkeys T and C after applying the spike thresholding and equalizing the spectral band powers, we averaged the SPC calculated across 100 repetitions per frequency band to attain a reliable measurement. Each repetition involved an independent random spike selection with an equal spike count threshold. To estimate the statistical significance of the SPC difference between the fast and slow trials in each frequency band, we used the sign test with Bonferroni correction for multiple comparisons. Additionally, for animals T and C, after finding the significant frequencies in each repetition, we counted the number of repetitions where each frequency's SPC difference was significant. A simple clustering method (K-means) was then applied on the set of the proportion values, to categorize them into two clusters with similar numbers. K-means categorizes n observations $(\mathbf{x}_1, \mathbf{x}_2, \ldots, \mathbf{x}_n)$ into $k(\le n)$ subsets $\mathbf{S} = \{s_1, s_2, \ldots, s_k\}$ so as to minimize the following objective function (99):

$$\arg\min_{\mathbf{S}} = \sum_{i=1}^{k} \sum_{\mathbf{x} \in S_i} \|\mathbf{x} - c_i\|^2, \qquad [2]$$

where c_i is a cluster center, calculated by the average of observation in S_i. Consequently, we considered the cluster of frequencies with the larger proportion values, as the significant frequencies. Finally, we tested if the two frequency clusters were significantly different in terms of their proportion values ($\rho < 10^{-5}$ for both monkeys, rank-sum test).

STA_{HG}. This control analysis was applied only on monkey H's data (which had enough number of trials/spikes). An identical procedure to the one described for the SPC analysis was performed to choose trials for this step. Consequently, all chosen trials included the same number of spikes (39 spikes). We further selected a subset of trials so that the LFP power (180 to 220 Hz) was the same between the fast and slow trials.

To represent the dynamics of high-gamma frequency band (180 to 220 Hz) over times around a spike event, all trials were fed to an FIR band-pass filter (implemented by EEGLAB's eegfilt function) to extract the high-gamma oscillation. Next, parts of the filtered LFP in a 30-ms time window surrounding the spikes of a trial were averaged across trials to form the STA_{HG}.

Histogram of the Average Instantaneous Phase. All trials having more than one spike in the analysis time window were considered to visualize the phase histograms. Moreover, the same number of trials was picked up from each of the fast and slow group. The LFPs were fed into a set of FIR filters (eegfilt) to pass the frequency range between 180–220 Hz (in 5 Hz wide frequency bands separated by 5 Hz steps). The Hilbert transform was then applied on the filtered LFPs to compute the instantaneous phases. Next, the phases

simultaneous to a trial's spikes were averaged circularly across the above frequency bands:

$$\overline{\varphi}_t = Arg\left\{\frac{1}{n}\sum_{j=1}^{n} e^{i\,\omega\,t_j}\right\},\ \omega = \{\,2\pi f|\ 180 \le f \le 220\ \text{Hz}\},\ -\pi \le \omega \le \pi, \qquad [3]$$

where $\overline{\varphi}_t$ is the circular average of high-gamma phase in a given trial t. Histograms show the distribution of these trials' corresponding circular average phases ($\overline{\varphi}_t$) in an RT condition for trials pooled across the three monkeys.

AUC Analysis. To perform the AUC analysis, SPC was calculated for the fast and slow trial groups where the target was shown inside or outside the RF, separately. After applying a moving average transform with a window length of 4, the AUC for the discrimination of fast and slow trials was computed across frequencies using the smoothed SPCs. AUC was estimated by using the logistic regression.

To characterize the frequencies with a significant difference in neural discrimination of RT between the target position conditions, we used a permutation test: The target position conditions in each fast/slow trial group were randomly shuffled 1,000 times. For each repetition per frequency band, we calculated the difference between the neural discrimination across the target position conditions. We next computed the proportion of repetitions with larger differences compared with the original difference. Those frequency bands with a proportion smaller than 0.05 are reported as frequencies with a significant influence of target position on neural discrimination of RT. Here, we corrected for multiple comparisons by ensuring that it is not likely to observe the significant frequency bands in succession ($P < 0.001$).

Analysis of STA_{HG} Across Electrode Distances. After averaging the STA_{HG}s, calculated within ±6-ms intervals surrounding the spikes across trials, the peak-to-peak amplitude difference was computed. The ±6-ms interval was selected based on the low cutoff (180 Hz) of the band-pass FIR filter. To reach a stable result, this analysis was averaged across 100 repetitions for each interelectrode distance.

Testing for the Spectral Leakage of Spike Waveform into LFP. We selected a subset of the fast and slow trials with at least 39 spikes in the analysis period and an equal average band power in the high-gamma frequency range (180 to 220 Hz). A similar routine as described for the SPC analysis was employed for choosing trials based on the same average spectral power. We next focused on the chosen fast trials. The STA_{LFP} as well as the STA_{HG} were calculated for each trial. The difference between the STA_{HG}'s peak-to-peak amplitudes of each trial was calculated within a ±8-ms interval around the spikes. After sorting the trials based on these peak-to-peak differences, we selected the first and last 87.5% as $FAST_{Low}$ and $FAST_{High}$ trials, respectively. The peak-to-peak amplitude difference for the two STA_{LFP} groups was computed for ±10-ms intervals surrounding the spikes. We selected this interval based on the leakage component's largest variation.

Availability of Data and Materials. The data underlying the result figures are publicly available (100).

ACKNOWLEDGMENTS. We thank Laura Busse and Steffen Katzner for sharing the data they recorded from monkey T. We also thank Dirk Prüsse, Leonore Burchardt, and Ralf Brockhausen for superb technical assistance and the DPZ's veterinary and animal husbandry staff for their expert animal care. This work was supported by grants from the Deutsche Forschungsgemeinschaft through the Collaborative Research Center 889 "Cellular Mechanisms of Sensory Processing" (Project C04, project number 154113120, to S.T.), the Federal Ministry of Education and Research (BMBF) of Germany under Grant 01GQ1005C, and the Iranian Cognitive Sciences and Technologies Council (Grant 4225, to M.B.K.).

1. C. Xue, D. Kaping, S. B. Ray, B. S. Krishna, S. Treue, Spatial attention reduces burstiness in macaque visual cortical area MST. *Cereb. Cortex* **27**, 83–91 (2017).
2. M. Esghaei, M. R. Daliri, S. Treue, Attention decreases phase-amplitude coupling, enhancing stimulus discriminability in cortical area MT. *Front. Neural Circuits* **9**, 82 (2015).
3. A. Palmigiano, T. Geisel, F. Wolf, D. Battaglia, Flexible information routing by transient synchrony. *Nat. Neurosci.* **20**, 1014–1022 (2017).
4. I. Grothe *et al*., Attention selectively gates afferent signal transmission to area V4. *J. Neurosci.* **38**, 3441–3452 (2018).
5. M. Esghaei, M. R. Daliri, S. Treue, Attention decouples action potentials from the phase of local field potentials in macaque visual cortical area MT. *BMC Biol.* **16**, 86 (2018).
6. W. H. Bosking, J. H. R. Maunsell, Effects of stimulus direction on the correlation between behavior and single units in area MT during a motion detection task. *J. Neurosci.* **31**, 8230–8238 (2011).
7. M. R. Cohen, J. H. R. Maunsell, A neuronal population measure of attention predicts behavioral performance on individual trials. *J. Neurosci.* **30**, 15241–15253 (2010).
8. M. R. Cohen, W. T. Newsome, Estimates of the contribution of single neurons to perception depend on timescale and noise correlation. *J. Neurosci.* **29**, 6635–6648 (2009).
9. E. P. Cook, J. H. R. Maunsell, Attentional modulation of behavioral performance and neuronal responses in middle temporal and ventral intraparietal areas of macaque monkey. *J. Neurosci.* **22**, 1994–2004 (2002).
10. F. O. Galashan, H. C. Saßen, A. K. Kreiter, D. Wegener, Monkey area MT latencies to speed changes depend on attention and correlate with behavioral reaction times. *Neuron* **78**, 740–750 (2013).
11. I. Kang, J. H. R. Maunsell, Potential confounds in estimating trial-to-trial correlations between neuronal response and behavior using choice probabilities. *J. Neurophysiol.* **108**, 3403–3415 (2012).
12. J. Lee, S. G. Lisberger, Gamma synchrony predicts neuron-neuron correlations and correlations with motor behavior in extrastriate visual area MT. *J. Neurosci.* **33**, 19677–19688 (2013).
13. J. Lee, M. Joshua, J. F. Medina, S. G. Lisberger, Signal, noise, and variation in neural and sensory-motor latency. *Neuron* **90**, 165–176 (2016).
14. J. Liu, W. T. Newsome, Local field potential in cortical area MT: Stimulus tuning and behavioral correlations. *J. Neurosci.* **26**, 7779–7790 (2006).
15. J. Liu, W. T. Newsome, Correlation between speed perception and neural activity in the middle temporal visual area. *J. Neurosci.* **25**, 711–722 (2005).
16. J. E. T. Smith *et al*., Dynamics of the functional link between area MT LFPs and motion detection. *J. Neurophysiol.* **114**, 80–98 (2015).
17. T. Womelsdorf, P. Fries, P. P. Mitra, R. Desimone, Gamma-band synchronization in visual cortex predicts speed of change detection. *Nature* **439**, 733–736 (2006).
18. A. Traschütz, A. K. Kreiter, D. Wegener, Transient activity in monkey area MT represents speed changes and is correlated with human behavioral performance. *J. Neurophysiol.* **113**, 890–903 (2015).
19. K. H. Britten, W. T. Newsome, M. N. Shadlen, S. Celebrini, J. A. Movshon, A relationship between behavioral choice and the visual responses of neurons in macaque MT. *Vis. Neurosci.* **13**, 87–100 (1996).
20. L. N. Katz, J. L. Yates, J. W. Pillow, A. C. Huk, Dissociated functional significance of decision-related activity in the primate dorsal stream. *Nature* **535**, 285–288 (2016).
21. K. Wimmer *et al*., Sensory integration dynamics in a hierarchical network explains choice probabilities in cortical area MT. *Nat. Commun.* **6**, 6177 (2015).
22. S. Katzner *et al*., Local origin of field potentials in visual cortex. *Neuron* **61**, 35–41 (2009).
23. N. K. Logothetis, The underpinnings of the BOLD functional magnetic resonance imaging signal. *J. Neurosci.* **23**, 3963–3971 (2003).
24. F. A. Khawaja, J. M. G. Tsui, C. C. Pack, Pattern motion selectivity of spiking outputs and local field potentials in macaque visual cortex. *J. Neurosci.* **29**, 13702–13709 (2009).
25. M. Esghaei, M. R. Daliri, S. Treue, Local field potentials are induced by visually evoked spiking activity in macaque cortical area MT. *Sci. Rep.* **7**, 17110 (2017).
26. M. Parto Dezfouli, M. B. Khamechian, S. Treue, M. Esghaei, M. R. Daliri, Neural activity predicts reaction in primates long before a behavioral response. *Front. Behav. Neurosci.* **12**, 207 (2018).
27. G. Buzsáki, Neural syntax: Cell assemblies, synapsembles, and readers. *Neuron* **68**, 362–385 (2010).
28. P. Fries, A mechanism for cognitive dynamics: Neuronal communication through neuronal coherence. *Trends Cogn. Sci.* **9**, 474–480 (2005).
29. T. M. Hall, K. Nazarpour, A. Jackson, Real-time estimation and biofeedback of single-neuron firing rates using local field potentials. *Nat. Commun.* **5**, 5462 (2014).
30. B. Voloh, T. Womelsdorf, A role of phase-resetting in coordinating large scale neural networks during attention and goal-directed behavior. *Front. Syst. Neurosci.* **10**, 18 (2016).
31. R. T. Canolty *et al*., Oscillatory phase coupling coordinates anatomically dispersed functional cell assemblies. *Proc. Natl. Acad. Sci. U.S.A.* **107**, 17356–17361 (2010).
32. C. Kayser, M. A. Montemurro, N. K. Logothetis, S. Panzeri, Spike-phase coding boosts and stabilizes information carried by spatial and temporal spike patterns. *Neuron* **61**, 597–608 (2009).
33. M. A. Montemurro, M. J. Rasch, Y. Murayama, N. K. Logothetis, S. Panzeri, Phase-of-firing coding of natural visual stimuli in primary visual cortex. *Curr. Biol.* **18**, 375–380 (2008).
34. T. Womelsdorf *et al*., Orientation selectivity and noise correlation in awake monkey area V1 are modulated by the gamma cycle. *Proc. Natl. Acad. Sci. U.S.A.* **109**, 4302–4307 (2012).
35. M. Siegel, M. R. Warden, E. K. Miller, Phase-dependent neuronal coding of objects in short-term memory. *Proc. Natl. Acad. Sci. U.S.A.* **106**, 21341–21346 (2009).
36. G. Dragoi, G. Buzsáki, Temporal encoding of place sequences by hippocampal cell assemblies. *Neuron* **50**, 145–157 (2006).
37. A. Fernández-Ruiz *et al*., Entorhinal-CA3 dual-input control of spike timing in the hippocampus by theta-gamma coupling. *Neuron* **93**, 1213–1226.e5 (2017).
38. C. Geisler *et al*., Temporal delays among place cells determine the frequency of population theta oscillations in the hippocampus. *Proc. Natl. Acad. Sci. U.S.A.* **107**, 7957–7962 (2010).
39. M. Vinck, T. Womelsdorf, E. A. Buffalo, R. Desimone, P. Fries, Attentional modulation of cell-class-specific gamma-band synchronization in awake monkey area v4. *Neuron* **80**, 1077–1089 (2013).
40. P. Berens, CircStat: A MATLAB toolbox for circular statistics. *J. Stat. Softw.* **31**, 1–21 (2009).

41. K. Li *et al*., Neurons in primate visual cortex alternate between responses to multiple stimuli in their receptive field. *Front. Comput. Neurosci.* **10**, 141 (2016).
42. S. Ray, S. S. Hsiao, N. E. Crone, P. J. Franaszczuk, E. Niebur, Effect of stimulus intensity on the spike-local field potential relationship in the secondary somatosensory cortex. *J. Neurosci.* **28**, 7334–7343 (2008).
43. B. O. Watson, M. Ding, G. Buzsáki, Temporal coupling of field potentials and action potentials in the neocortex. *Eur. J. Neurosci.* **48**, 2482–2497 (2018).
44. G. Buzsáki, *Rhythms of the Brain* (Oxford University Press, 2006), pp. 136–160.
45. M. D. McDonnell, D. Abbott, What is stochastic resonance? Definitions, misconceptions, debates, and its relevance to biology. *PLoS Comput. Biol.* **5**, e1000348 (2009).
46. D. Guo, M. Perc, Y. Zhang, P. Xu, D. Yao, Frequency-difference-dependent stochastic resonance in neural systems. *Phys. Rev. E* **96**, 022415 (2017).
47. C.-C. Chang, C.-J. Lin, LIBSVM: A library for support vector machines. *ACM Trans. Intell. Syst. Technol.* **2**, 1–27 (2011).
48. G. Buzsáki, A. Draguhn, Neuronal oscillations in cortical networks. *Science* **304**, 1926–1929 (2004).
49. F. Darvas, K. J. Miller, R. P. N. Rao, J. G. Ojemann, Nonlinear phase-phase cross-frequency coupling mediates communication between distant sites in human neocortex. *J. Neurosci.* **29**, 426–435 (2009).
50. S. E. Folias, S. Yu, A. Snyder, D. Nikolić, J. E. Rubin, Synchronisation hubs in the visual cortex may arise from strong rhythmic inhibition during gamma oscillations. *Eur. J. Neurosci.* **38**, 2864–2883 (2013).
51. M. N. Havenith *et al*., Synchrony makes neurons fire in sequence, and stimulus properties determine who is ahead. *J. Neurosci.* **31**, 8570–8584 (2011).
52. J. Ito, P. Maldonado, W. Singer, S. Grün, Saccade-related modulations of neuronal excitability support synchrony of visually elicited spikes. *Cereb. Cortex* **21**, 2482–2497 (2011).
53. B. C. Lewandowski, M. Schmidt, Short bouts of vocalization induce long-lasting fast γ oscillations in a sensorimotor nucleus. *J. Neurosci.* **31**, 13936–13948 (2011).
54. F. Varela, J.-P. Lachaux, E. Rodriguez, J. Martinerie, The brainweb: Phase synchronization and large-scale integration. *Nat. Rev. Neurosci.* **2**, 229–239 (2001).
55. J. H. Siegle, D. L. Pritchett, C. I. Moore, Gamma-range synchronization of fast-spiking interneurons can enhance detection of tactile stimuli. *Nat. Neurosci.* **17**, 1371–1379 (2014).
56. L. L. Colgin *et al*., Frequency of gamma oscillations routes flow of information in the hippocampus. *Nature* **462**, 353–357 (2009).
57. G. G. Gregoriou, S. J. Gotts, H. Zhou, R. Desimone, High-frequency, long-range coupling between prefrontal and visual cortex during attention. *Science* **324**, 1207–1210 (2009).
58. G. Buzsáki, C. A. Anastassiou, C. Koch, The origin of extracellular fields and currents–EEG, ECoG, LFP and spikes. *Nat. Rev. Neurosci.* **13**, 407–420 (2012).
59. E. A. Buffalo, P. Fries, R. Landman, T. J. Buschman, R. Desimone, Laminar differences in gamma and alpha coherence in the ventral stream. *Proc. Natl. Acad. Sci. U.S.A.* **108**, 11262–11267 (2011).
60. Y. Cabral-Calderin, C. Schmidt-Samoa, M. Wilke, Rhythmic gamma stimulation affects bistable perception. *J. Cogn. Neurosci.* **27**, 1298–1307 (2015).
61. A. K. Engel, W. Singer, Temporal binding and the neural correlates of sensory awareness. *Trends Cogn. Sci.* **5**, 16–25 (2001).
62. Y. Nir *et al*., Interhemispheric correlations of slow spontaneous neuronal fluctuations revealed in human sensory cortex. *Nat. Neurosci.* **11**, 1100–1108 (2008).
63. R. Mukamel *et al*., Coupling between neuronal firing, field potentials, and FMRI in human auditory cortex. *Science* **309**, 951–954 (2005).
64. K. J. Miller *et al*., Broadband changes in the cortical surface potential track activation of functionally diverse neuronal populations. *Neuroimage* **85**, 711–720 (2014).
65. M. A. Gieselmann, A. Thiele, Comparison of spatial integration and surround suppression characteristics in spiking activity and the local field potential in macaque V1. *Eur. J. Neurosci.* **28**, 447–459 (2008).
66. S. Ray, J. H. R. Maunsell, Different origins of gamma rhythm and high-gamma activity in macaque visual cortex. *PLoS Biol.* **9**, e1000610 (2011).
67. X. Jia, D. Xing, A. Kohn, No consistent relationship between gamma power and peak frequency in macaque primary visual cortex. *J. Neurosci.* **33**, 17–25 (2013).
68. R. L. T. Goris, J. A. Movshon, E. P. Simoncelli, Partitioning neuronal variability. *Nat. Neurosci.* **17**, 858–865 (2014).
69. K. S. Chaisanguanthum, M. Joshua, J. F. Medina, W. Bialek, S. G. Lisberger, The neural code for motor control in the cerebellum and oculomotor brainstem. *eNeuro* **1**, ENEURO.0004-14.2014 (2014).
70. G. Buzsáki, Z. Horváth, R. Urioste, J. Hetke, K. Wise, High-frequency network oscillation in the hippocampus. *Science* **256**, 1025–1027 (1992).
71. J. Csicsvari, H. Hirase, A. Mamiya, G. Buzsáki, Ensemble patterns of hippocampal CA3-CA1 neurons during sharp wave-associated population events. *Neuron* **28**, 585–594 (2000).
72. A. Ylinen *et al*., Sharp wave-associated high-frequency oscillation (200 Hz) in the intact hippocampus: Network and intracellular mechanisms. *J. Neurosci.* **15**, 30–46 (1995).
73. P. Billeke *et al*., Brain state-dependent recruitment of high-frequency oscillations in the human hippocampus. *Cortex* **94**, 87–99 (2017).
74. A. Bragin, J. Engel, Jr, C. L. Wilson, I. Fried, G. Buzsáki, High-frequency oscillations in human brain. *Hippocampus* **9**, 137–142 (1999).
75. N. Brunel, X.-J. Wang, What determines the frequency of fast network oscillations with irregular neural discharges? I. Synaptic dynamics and excitation-inhibition balance. *J. Neurophysiol.* **90**, 415–430 (2003).
76. J. A. Henrie, R. Shapley, LFP power spectra in V1 cortex: The graded effect of stimulus contrast. *J. Neurophysiol.* **94**, 479–490 (2005).
77. E. Stark *et al*., Pyramidal cell-interneuron interactions underlie hippocampal ripple oscillations. *Neuron* **83**, 467–480 (2014).
78. P. Suffczynski, N. E. Crone, P. J. Franaszczuk, Afferent inputs to cortical fast-spiking interneurons organize pyramidal cell network oscillations at high-gamma frequencies (60-200 Hz). *J. Neurophysiol.* **112**, 3001–3011 (2014).
79. A. Belitski *et al*., Low-frequency local field potentials and spikes in primary visual cortex convey independent visual information. *J. Neurosci.* **28**, 5696–5709 (2008).
80. G. Dragoi, S. Tonegawa, Preplay of future place cell sequences by hippocampal cellular assemblies. *Nature* **469**, 397–401 (2011).
81. A. C. Singer, M. F. Carr, M. P. Karlsson, L. M. Frank, Hippocampal SWR activity predicts correct decisions during the initial learning of an alternation task. *Neuron* **77**, 1163–1173 (2013).
82. D. Khodagholy, J. N. Gelinas, G. Buzsáki, Learning-enhanced coupling between ripple oscillations in association cortices and hippocampus. *Science* **358**, 369–372 (2017).
83. M. T. Kucewicz *et al*., High frequency oscillations are associated with cognitive processing in human recognition memory. *Brain* **137**, 2231–2244 (2014).
84. S. Ray, J. H. R. Maunsell, Network rhythms influence the relationship between spike-triggered local field potential and functional connectivity. *J. Neurosci.* **31**, 12674–12682 (2011).
85. R. Scheffer-Teixeira, H. Belchior, R. N. Leão, S. Ribeiro, A. B. L. Tort, On high-frequency field oscillations (>100 Hz) and the spectral leakage of spiking activity. *J. Neurosci.* **33**, 1535–1539 (2013).
86. G. Spyropoulos, C. A. Bosman, P. Fries, A theta rhythm in macaque visual cortex and its attentional modulation. *Proc. Natl. Acad. Sci. U.S.A.* **115**, E5614–E5623 (2018).
87. C. E. Schroeder, P. Lakatos, The gamma oscillation: Master or slave? *Brain Topogr.* **22**, 24–26 (2009).
88. A. Matsumoto *et al*., Pathological and physiological high-frequency oscillations in focal human epilepsy. *J. Neurophysiol.* **110**, 1958–1964 (2013).
89. N. Axmacher, C. E. Elger, J. Fell, Ripples in the medial temporal lobe are relevant for human memory consolidation. *Brain* **131**, 1806–1817 (2008).
90. P. R. Roelfsema, S. Treue, Basic neuroscience research with nonhuman primates: A small but indispensable component of biomedical research. *Neuron* **82**, 1200–1204 (2014).
91. M. Berger *et al*., Standardized automated training of rhesus monkeys for neuroscience research in their housing environment. *J. Neurophysiol.* **119**, 796–807 (2018).
92. A. Calapai *et al*., A cage-based training, cognitive testing and enrichment system optimized for rhesus macaques in neuroscience research. *Behav. Res. Methods* **49**, 35–45 (2017).
93. D. Pfefferle, S. Plümer, L. Burchardt, S. Treue, A. Gail, Assessment of stress responses in rhesus macaques (Macaca mulatta) to daily routine procedures in system neuroscience based on salivary cortisol concentrations. *PLoS One* **13**, e0190190 (2018).
94. M. Esghaei, M. R. Daliri, Decoding of visual attention from LFP signals of macaque MT. *PLoS One* **9**, e100381 (2014).
95. S. Katzner, L. Busse, S. Treue, Attention to the color of a moving stimulus modulates motion-signal processing in macaque area MT: Evidence for a unified attentional system. *Front. Syst. Neurosci.* **3**, 12 (2009).
96. M. C. Aoi, K. Q. Lepage, M. A. Kramer, U. T. Eden, Rate-adjusted spike-LFP coherence comparisons from spike-train statistics. *J. Neurosci. Methods* **240**, 141–153 (2015).
97. J. F. Mitchell, K. A. Sundberg, J. H. Reynolds, Spatial attention decorrelates intrinsic activity fluctuations in macaque area V4. *Neuron* **63**, 879–888 (2009).
98. B. Pesaran *et al*., Investigating large-scale brain dynamics using field potential recordings: Analysis and interpretation. *Nat. Neurosci.* **21**, 903–919 (2018).
99. J. Macqueen, "Some methods for classification and analysis of multivariate observations" in *Proceedings of the Fifth Berkeley Symposium on Mathematical Statistics and Probability,* L. M. Le Cam, J. Neyman, Eds. (University of California Press, Berkeley, CA, 1967), pp. 281–297.
100. M. B. Khamechian, V. Kozyrev, S. Treue, M. Esghaei, M. R. Daliri, Data from "Routing information flow by separate neural synchrony frequencies allows for functionally labeled lines in higher primate cortex (Data underlying result figures)." figshare, 10.6084/m9.figshare.8160029. Deposited 21 May 2019.